Research Articles   Research Administration

2018

A framework for intracranial saccular aneurysm detection and quantification using morphological analysis of cerebral angiograms

K Malik

S Anjum

Hamid Soltanian-Zadeh
Henry Ford Health, Hsoltan1@hfhs.org

H Malik

G Malik

Recommended Citation

A Framework for Intracranial Saccular Aneurysm Detection and Quantification using Morphological Analysis of Cerebral Angiograms

KHALID MAHMOOD MALIK[1], **SHAKEEL M. ANJUM**[2], **HAMID SOLTANIAN-ZADEH**[3], **HAFIZ MALIK**[4], **AND GHAUS M. MALIK**[5]

[1]Department of Computer Science and Engineering, Oakland University, Rochester, MI 48309 USA
[2]Computer Science Department, FAST–National University of Computer and Emerging Sciences, Faisalabad 38000, Pakistan
[3]Medical Image Analysis Laboratory, Department of Radiology and Research Administration, Henry Ford Health System, Detroit, MI 48202 USA
[4]Electrical and Computer Engineering Department, University of Michigan–Dearborn, Dearborn, MI 48128 USA
[5]Henry Ford West Bloomfield Hospital, West Bloomfield Township, MI 48322 USA

Corresponding author: Khalid Mahmood Malik (mahmood@oakland.edu)

ABSTRACT Reliable early prediction of aneurysm rupture can greatly help neurosurgeons to treat aneurysms at the right time, thus saving lives as well as providing significant cost reduction. Most of the research efforts in this respect involve statistical analysis of collected data or simulation of hemodynamic factors to predict the risk of aneurysmal rupture. Whereas, morphological analysis of cerebral angiogram images for locating and estimating unruptured aneurysms is rarely considered. Since digital subtraction angiography (DSA) is regarded as a standard test by the American Stroke Association and American College of Radiology for identification of aneurysm, this paper aims to perform morphological analysis of DSA to accurately detect saccular aneurysms, precisely determine their sizes, and estimate the probability of their ruptures. The proposed diagnostic framework, intracranial saccular aneurysm detection and quantification, first extracts cerebrovascular structures by denoising angiogram images and delineates regions of interest (ROIs) by using watershed segmentation and distance transformation. Then, it identifies saccular aneurysms among segmented ROIs using multilayer perceptron neural network trained upon robust Haralick texture features, and finally quantifies aneurysm rupture by geometrical analysis of identified aneurysmic ROI. De-identified data set of 59 angiograms is used to evaluate the performance of algorithms for aneurysm detection and risk of rupture quantification. The proposed framework achieves high accuracy of 98% and 86% for aneurysm classification and quantification, respectively.

INDEX TERMS Computer-assisted diagnosis, digital subtraction angiography (DSA), intracranial saccular aneurysm, rupture quantification, Haralick features, GLCM, GLRLM, multilayer perceptron (MLP) neural network.

I. INTRODUCTION

Higher mortality and morbidity rates among aneurysmic patients due to intracerebral ruptures have added to the necessity of detecting and analyzing unruptured intracranial aneurysms. An intracranial or cerebral aneurysm is a condition in which a blood vessel starts swelling outwards and gradually bulges out like a balloon due to weakness in a blood vessel's wall, as shown in Fig. 1(a). growth in aneurysm size evokes the risk of rupture due to increased pressure of blood on the ballooned area and remains asymptomatic until over-sized. Eventually if an aneurysm bursts, it causes aneurysmal Subarachnoid Hemorrhage (aSAH), a damaging flow of blood into the cerebra. Statistics reveal that in the

USA alone over six million brain aneurysms are diagnosed every year and 30,000 of them rupture [1]. Damages from aSAH vary from severe disability to spontaneous death and it occurs relatively more at young age as compared to other types of stroke [2]. Statistics show that 50% of patients with ruptured aneurysms die before reaching the hospital and the remaining 50% die within the next 24 months even if taken through invasive surgical treatments, because of re-bleeding or deficits caused by the initial burst [3]. Furthermore, among different forms of intracranial aneurysms, i.e. fusiform, distal and dissection, saccular aneurysms (so named for their berry or sac-like shape) are characterized as the most vulnerable to fast growth and rupture. Ruptured saccular
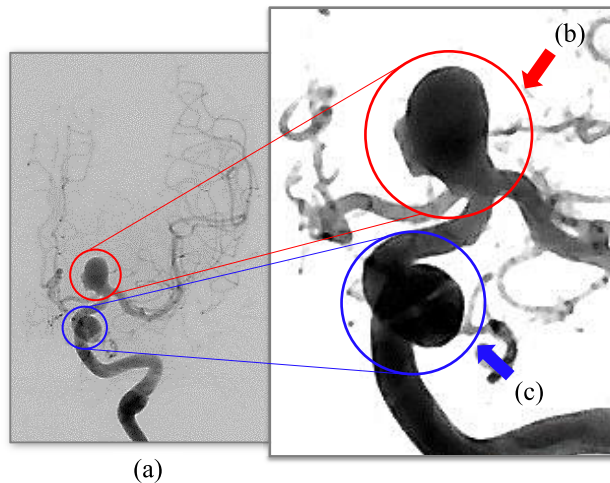
FIGURE 1. (a) Cerebral Angiogram, (b) Saccular Aneurysm, (c) Arterial Loop.

aneurysms account for roughly 80% of aSAH whereas other types of cerebral aneurysms typically grow more slowly and rupture less frequently [1], [10].

Neurosurgeons experience various difficulties in accurately detecting and treating cerebral aneurysms. Therefore, it is important to identify aneurysms and differentiate them from vasculature loops without unnecessary magnetic resonance angiography (MRA), computerized tomography angiography (CTA), and DSA. In patients with unruptured aneurysms, the treatment decision is very complicated because not all intracranial aneurysms are destined to rupture, however, in case of rupture, the consequences are devastating. On the other hand, surgical treatment (clipping) or endovascular coiling of unreptured aneurysm also carries a combined risk of up to 5%, for treatment-related fatality and morbidity [3], besides high financial cost. Thus, the risks of treatment have to be balanced cautiously against the risk of rupture [7]. A satisfactory solution can only be based on individualization of the rupture risk. However, the prediction of aneurysm rupture, based on combination of risk factors is a complex problem, and a reliable clinical computer-assisted tool for its diagnosis does not exist.

In clinical practice, depending on the situation and purpose, a subset of MRA, DSA, and CTA is used to study prognostic factors for aneurysm rupture. Therefore, computer aided analysis of these artifacts is being rigorously investigated [8], [12], [23], [42]. Brain angiography images i.e. DSA, presented in Fig. 1(a), are considered as a standard test by the American Stroke Association and American College of Radiology for detection and estimation of cerebral aneurysms because they provide maximum contrast between cerebrovascular arteries and brain tissues [25]. This study aims to detect saccular aneurysm accurately and then quantify its rupture score precisely, that would act as a baseline for studying its growth rate using CTA and MRA in future. Moreover, to the best of our knowledge, literature rarely cites an inclusive effort on computer-assisted diagnosis (CAD) of

brain aneurysms based on DSA. This paper presents a novel framework, the Intracranial Saccular Aneurysm Detection and Quantification (ISADAQ), which articulates a comprehensive investigation of cerebral angiograms for estimation of aneurysm rupture score.

Visual inspection of DSA poses following design challenges which ISADAQ is intended to surmount:

1) Angiograms taken at different medical facilities carry varying dimensionalities and signal to noise ratios, which hinder automated detection of saccular aneurysms. The problem of normalizing and denoising angiograms becomes important because subsequent morphological analysis depends on correct extraction of vasculature from angiograms.

2) Brain arteries are inherently complex and discriminating between malignant aneurysmal lesions from healthy arterial details, like loops and overlays, is not straight forward. Defining a set of unique visual features of saccular aneurysms and training a system based on them that accurately detects their presence in an angiogram with high sensitivity is nontrivial because sometimes it is even difficult for radiologists and neurosurgeons to distinguish aneurysms from rest of the vasculature.

3) Precise estimations of a saccular aneurysm's size, relative aspect ratios and prediction of rupture are the most demanding tasks of an automated diagnosis system because they help physicians to validate their critical treatment decisions for initial detection and growth of intracranial saccular aneurysms.

Considering the aforementioned clinical challenges, the main contributions of the ISADAQ framework include: *i)* denoising angiograms for accurate extraction of cerebrovascular structures and watershed segmentation for delineation of candidate regions of interest (ROIs) based on points of interest (POIs) calculated as local maxima of distance transformed image, *ii)* identification of saccular aneurysm among the segmented ROIs through Multilayer Perceptron (MLP) neural network trained on robust Haralick textural features which are not easily perceptible by the human eye but are computed from the Gray-level Co-occurrence Matrix (GLCM), and *iii)* estimation of aneurysm rupture probability in terms of the proposed BASSH score (*i.e. b*ottleneck ratio, *a* spect ratio, *s*ize ratio, *s*urface area, and *h* emodynamic factor), calculated from size and shape indices of detected aneurysmal segment and geometrical analysis of its local and spatial attributes. Moreover, the performance of MLPNN classification is evaluated in terms of network robustness and efficiency by varying input data and parameters.

The rest of this paper is organized as follows: *Section II* describes the current state-of-the-art by citing related research work and *Section III* provides a detailed overview of the ISADAQ architecture and describes the functionality of each module. To explain the complex sequence of morphological analysis, we explain each phase by processing

an angiogram image having one saccular aneurysm, shown in Fig. 1(b), and an indistinct arterial loop, shown in Fig. 1(c). *Section IV* presents experimental results and performance evaluation of our proposed framework in terms of robustness and efficiency. Finally, *Section V* concludes the paper and highlight some future directions.

II. RELATED WORK

In recent years, computer-assisted diagnosis (CAD) schemes focused on manual or semi-automated detection and size estimation of Intracranial Aneurysm (IA) for imaging modalities like MRA and CTA. However, automated analysis of DSA, despite its being the most authentic and standard means of cerebral aneurysm detection and rupture risk quantification, remained unexplored. A recent study on CAD systems for diagnostic analysis of cerebral disorders [6] explored the challenges and demands of accumulating, managing, and analyzing medical big data for computer-assisted diagnosis of neurological abnormalities. This work has foregrounded the need to devise technologies for analysis of large volumes of data available in imaging modalities like MRI, CT, and PET to automate diagnosis of neurological disorders like epilepsy, Alzheimer's, Parkinson's, dementia, autism, and tumor, without even mentioning intracranial aneurysms. On the other hand, several studies have dealt with individual aspects of automated diagnosis of cerebral aneurysm using multimodal imaging data including DSA [25], [28], [43]. To the best of our knowledge, none of these efforts has investigated DSA comprehensively to devise a CAD system to generate reliable, qualitative and quantitative diagnostic results for aneurysms and predict their rupture probability.

Estimation of an overall risk score for aneurysm rupture in a patient based on a combination of critical risk factors is known to be very difficult. Our literature review shows that there is a recent surge of interest in intracranial aneurysm rupture quantification through statistical analysis of clinical data-points. The studies in this regard include estimation of rupture by developing the PHASES and ELAPSS scores [5], [9], [38], which quantify aneurysm rupture status through statistical analysis of patients' health records in terms of earlier subarachnoid hemorrhage history, population, hypertension, age, and aneurysm size and location. However, without considering the complex phenomenon of various shapes (smooth saccular, irregular saccular, fusiform, dissection, distal, and complex) and specific imaging modalities (DSA, CTA, and MRA), these models suffer from bias, inaccuracy, and insufficiency of clinical data. While they may work for preliminary observations or follow up studies, they are not suitable for critical decision making at the time of aneurysm detection and treatment. The proposed BASSH score incorporates critical anatomical characteristics to accurately estimate aneurysm rupture through morphological analysis of DSA images.

Automated analysis of brain images can be segregated into segmentation, classification, and quantification problems. Earlier inspections of CTA and MRA images aimed at segmentation of vascular structures into blood vessels and brain tissues through morphological characterization [12], [15], [44], [45]. The study estimated aneurysms' completeness and orthonormality factors by applying vascular skeletonization to isolate aneurysms [14]. Geometrical and Zernike moment invariants define a limited set of global shape descriptors to accurately delineate aneurysmal segments. Overcoming the limitations of prior approaches for segmentation of CTA images, the authors extended the framework for MRA images using machine learning based classification techniques [20]. The methodology comprised of, *i)* regions of interest (ROIs) segmentation through skeleton processing, *ii)* aneurysm dome isolation using centerline and ostium detection, and *iii)* aneurysm quantification based on aspect ratio, volume, and surface area. The performance of the proposed technique was evaluated using images from only 10 patients. Through analysis of changes in boundary pixel intensities of PC-MRA images, intracranial vessels and aneurysms are segmented in [26]. This scheme computes intensity discontinuity descriptors and intensity variance quantifiers. Without training a classifier to determine boundary lines of a vascular phantom, the segmentation technique is unable to accurately isolate aneurysmal voxels from arterial loops, generating a large number of false positives (44% calculated from the results presented for 5 PC-MRA images).

Recently, sphere enhancement filters were applied to various cerebral image modalities (2DRA, CTA, MRA, and DSA) to facilitate computer-aided classification of smaller intracranial aneurysms [41], [44]. The authors computed the ratio of Hessian eigenvalues (e.g., lymbda1, Sato's, Frangi's, Li's) to detect saccular aneurysms smaller than 4 mm. The algorithm achieved relatively high accuracy of classification but with limited recognition: it detected only small saccular aneurysms instead of larger ones that are more susceptible to rupture. Based on the former studies, two similar investigations [24], [25] calculated local maxima from multiple images modalities (CTA and MRA) to automatically detect saccular aneurysms from normalized brain images but applying blob enhancement filters or K-means clustering of local maxima did not produce consistent results for recognition of variable aneurysm shapes. In [29], an edge density histogram is computed to extract shape features from medical images of the brain and lungs. With a precision of 0.523 for classifying the brain images, the reliability of this proposed edge-based multi-scale structuring element as a shape descriptor remains questionable. Among very few investigations regarding classification of arterial segments of 2D-DSA, one group devised a saccular aneurysm detection scheme by applying Fuzzy Mathematical Morphology (FMM) on vasculature extracted through fusion of two classifiers, FCM (Fuzzy C-Means) and FKNN (Fuzzy K-Nearest Neighbors) [28]. Although the idea of extracting arterial structure from DSA images by classifying individual pixels seems convincing, the reliability of the FMM classifier is questionable because it uses a very small dataset including 2-3 experimental images.

Another study presented a generic pixel intensity-based segmentation technique which could be trained to classify pixels of a diverse range of imaging modalities among intracranial vessels or aneurysmal segments [16]. The major setback of the proposed pixel segmentation techniques is that they lack the consideration of inter-pixel relationship exhibited by the specific shape of an aneurysm. A recent study [27] investigated multi-sequence MRI images of cirrhotic brain disease and extracted texture features like GLCM. The methodology trains an artificial neural network (ANN) using GLCM and classifies ROIs with high sensitivity. The authors endorse the usage of texture features for classification of other kinds of malignant brain lesions, such as aneurysms.

Alongside morphological characterization, several statistical models have been proposed to develop a set of features to accurately quantify aneurysm rupture risk. To this end, a biomathematical model built upon historical data of unruptured saccular aneurysms using binary logistic regression suggests that the height, width, and neck size of aneurysms are the most significant factors to be considered when quantifying the risk of rupture [22], [27]. Similarly, multivariate regression analysis of serial MRA images highlights that size is a significant predictor in prediction of aneurysm growth and rupture [4], [10]. It is clear that statistical findings need to be studied in more detail for geometrical factors other than surface area and diameter to arrive at a reliably robust model. Another effort in this respect cites a thorough statistical analysis of ruptured and unruptured intracranial aneurysms performed on a dataset comprised of 27 CTA scans [15]. Their analysis suggests that an aneurysm's shape indices (aspect ratio, bottleneck factor, non-sphericity index, ellipticity index, etc.) are more effective in quantifying rupture probability than size indices (height, width, volume, surface area, etc.). We therefore conclude that little comprehensive effort has been devoted to identification of the most significant geometrical parameters for aneurysm rupture score estimation after accurate detection of aneurysmal regions of interest.

The following section explains our proposed methodology through a pilot run on morphological, anatomical, and textural analysis of angiograms (DSA). The encouraging results of our classification and estimation schemes establish their viability for extension to other imaging modalities in future.

III. MATERIALS AND METHODOLOGY

A. DATA COLLECTION

The lack of any publicly accessible anonymized dataset of angiogram images containing saccular brain aneurysms was a crucial problem for a systematic morphological analysis. We acquired 59 phase-contrast digital subtraction angiograms of 34 patients from Henry Ford Hospital, Bloomfield Hills, MI, USA (IRB approval No. 11254). Patients' angiograms and other clinical data was anonymized before analysis. The data consisted of 47 angiograms with a single saccular aneurysm and 12 angiograms with no aneurysms. The saccular aneurysms ranged in size from 6 mm to 21 mm, and images with multiple aneurysms and fusiform or dissecting types were excluded to limit the scope of this work.

B. PARAMETER SELECTION

Cerebral angiograms possess local pixel intensity patterns which can efficaciously describe geometrical consistency of the brain's arterial structure after specific morphological treatment. Such distinctive textural characteristics are of primary interest to our classification technique because they collect discrete grayscale tonal primitives of image segments, for instance, fourteen *Haralick* features are computed to characterize pathologically different regions of cerebral angiograms. These exclusive statistical parameters, including contrast, correlation, energy, entropy, homogeneity, and variance, are derived from the 2nd-order GLCM.

Another set of features selected for size estimation of saccular aneurysm consists of morphological parameters, which accurately quantify the risk of aneurysmal rupture. These factors involve salient geometrical measurements of aneurysms' local and spatial characteristics which are consentient among several statistical investigations [10], [12], [14], [15]. Local anatomical features included aneurysm's neck diameter (D_n), its perpendicular height from neck (H), maximum height (H_{max}), maximum width (W), and average diameter of connecting artery (D_{avg}). Based on these scalar attributes, spatial factors are computed to predict the rupture score (ε), e.g., bottleneck factor (μ), aspect ratio (λ), size ratio (δ), surface area (Ω), and hemodynamic factor (ƒ).

C. PROPOSED FRAMEWORK – ISADAQ

The proposed methodology of processing a suspect angiogram through ISADAQ is shown in Fig. 2 and outlined as follows:

i) PRE-PROCESSING

The natural complexity of cerebrovascular topology adds to the intricacy of discriminating aneurysms from indistinct arterial structures. Therefore, ISADAQ substantively denoises background signals and extracts pixels of blobs and arteries.

ii) SEGMENTATION

The framework delineates arterial structure into candidate segments of interest by employing region-based, edge-based, and component-based segmentations to extract geometrical features for classification of arterial segments.

iii) CLASSIFICATION

ISADAQ trains feed-forward, a back propagation Multilayer Perceptron (MLP) Neural Network using salient textural features of the segmented regions. *Section C.3* explains how ISADAQ calculates the 2nd-order statistical features of each ROI using GLCM and computes its Haralick textural features. An MLP artificial neural network is trained using the extracted feature vectors which are annotated with ground
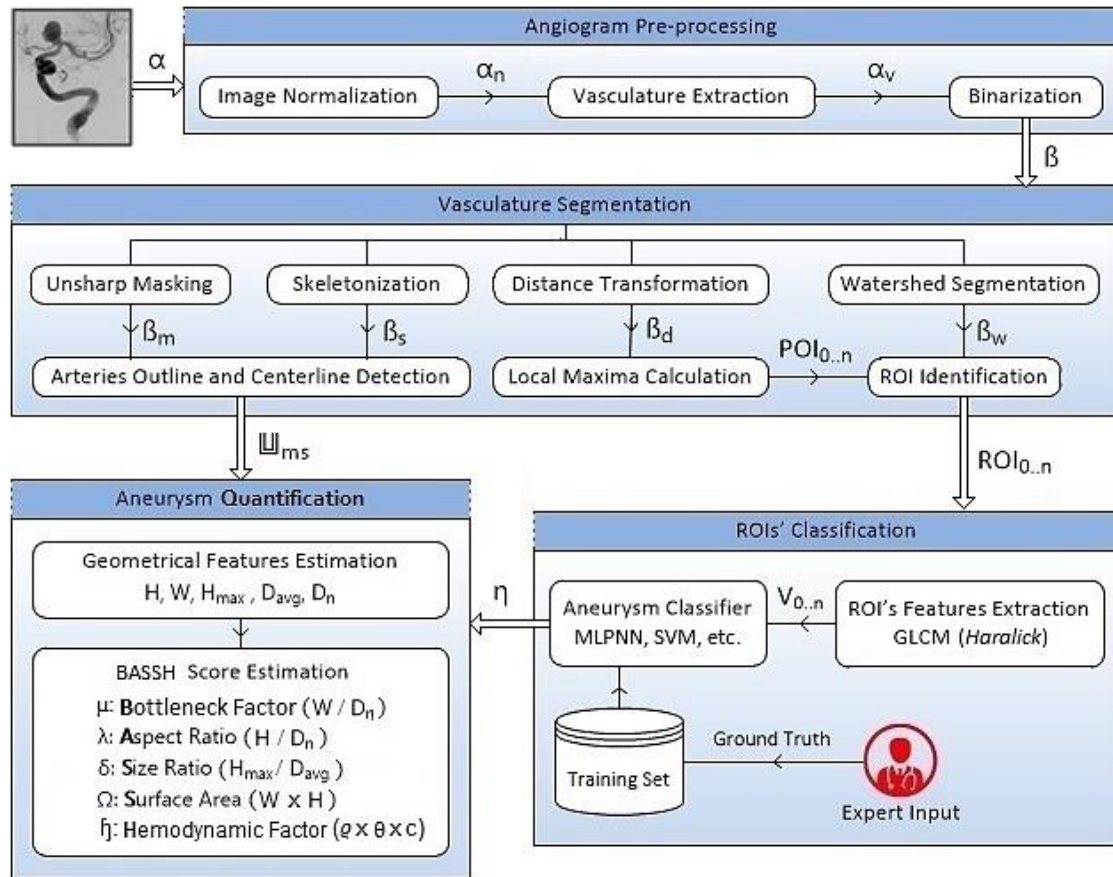
FIGURE 2. Architecture of Proposed Framework, Intracranial Saccular Aneurysm Detection and Quantification (ISADAQ).

truth established by expert radiologists to classify them into *malignant* (saccular aneurysms) and *benign* (non-aneurysmic) regions. *Section C.3* presents the experimental results of this classification.

iv) QUANTIFICATION

The framework calculates the rupture score of aneurysmal segments based on their geometric attributes. ISADAQ computes a BASSH score to estimate the probability of aneurysmal rupture, using basic visual characteristics (height, width, neck width, and artery diameter) extracted by morphological analysis of aneurysm geometry. Our size estimation and quantification technique is explained in *Section C.4.*

1) ANGIOGRAM PRE-PROCESSING

The proposed pre-processing algorithm consists of three phases: image normalization, vasculature extraction, and binarization. The details of each phase are given below.

a: IMAGE NORMALIZATION

The inherent signal-to-noise ratio and indistinctness of the arterial anatomy in angiograms pose unique challenges to morphological and geometrical analysis. Angiograms captured at different medical facilities through a diverse range

of scanning equipment have variable pixel densities and resolutions, between 1024px $\times$ 1024px to 2448px $\times$ 3264px. Therefore, normalization of pixel intensities before efficient foreground extraction and accurate segmentation is inevitable. The proposed pre-processing algorithm processes the input angiogram image α through a series of morphological operations to reduce overall computational complexity and to standardize image resolution.

Angiogram normalization starts by dimensionality reduction of the input image in terms of size and color. High resolution angiogram images are resized to 1024px $\times$ 1024px and a gray scale image is obtained from the RGB channels to simplify the morphological calculations. The disparity among the gray scale distributions is adjusted by applying global histogram equalization. Compared to adaptive histogram equalization, global histogram equalization better distributes spatial color surface across the output image α_n and results in an enhanced histogram that exhibits more differentiable disparity between foreground and background signals for further processing.

b: VASCULATURE EXTRACTION

There is a significant amount of noise in the normalized angiogram α_n, as shown in Fig. 3(a). To extract foreground
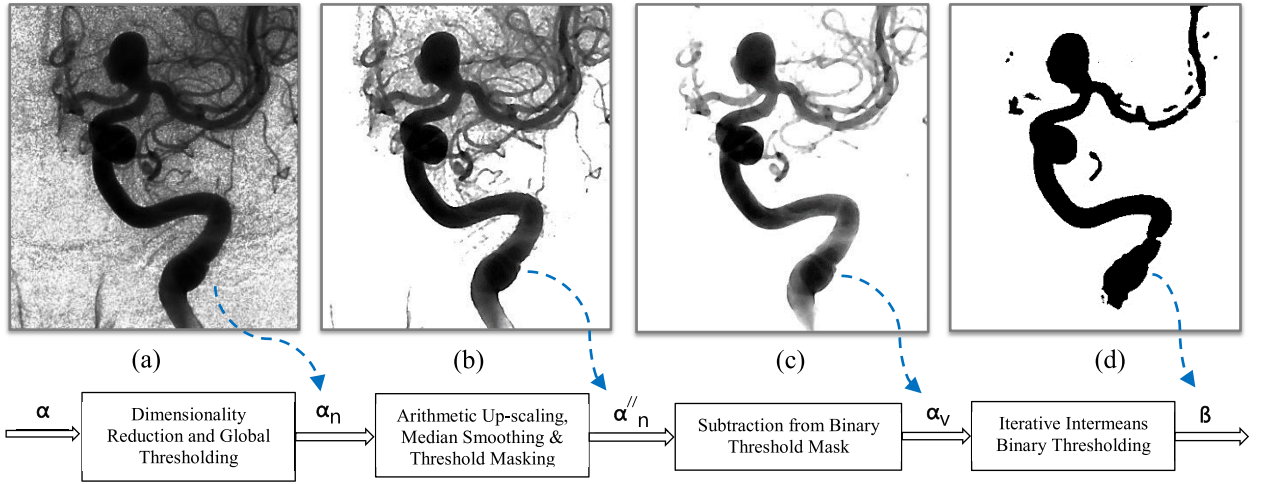
FIGURE 3. Vasculature Extraction and Binarization.

arterial surfaces, the noise needs to be suppressed. ISADAQ attenuates noise based on a very simple yet efficient arithmetic up-scaling operation followed by median filtering. Arithmetic up-scaling, as defined in (3), is performed on the input image α_n by multiplying every pixel with a constant c. Equations (1) and (2) calculate the multiplication constant $c = (\alpha_{max}/\alpha_{mean})$ as the ratio of the maximum and mean of the gray scale values in α_n. Moreover, the up-scaled pixel intensities for the output image α'_n are truncated at α_{max}.

$$\alpha_{max} = \gamma\{\alpha_n \in \alpha_n(x,y), x = 0,\ldots,n, y = 0,\ldots,m\}$$
$$0 \le \alpha_{max} \le 255 \quad (1)$$

$$\alpha_{mean} = \sum_{x=0,y=0}^{x=w-1,y=h-1} \alpha_n[x,y] \in z \quad (2)$$

where γ is the function that computes the mean value over a sliding window z of size 3×3 around a center point $\alpha_n[x,y]$ in image α_n.

$$\alpha'_n(x,y) = \sigma\{\alpha_n(x,y) \times c, \alpha_{max}\} \quad (3)$$

where c is calculated as the arithmetic upscaling factor and σ is the truncating function.

The resultant image α'_n reduces most of the background noise by adding natural brightness to the image intensities while preserving the relative contrast between the regions of the image. α'_n is further denoised by passing through the non-linear median filter, which removes remaining impulse noise by scanning every input pixel $\alpha'_n[x,y]$:

$$\alpha''_n(x,y) = \lambda\{\alpha'_n[x,y], (x,y) \in z\} \quad (4)$$

where λ computes the median over a sliding window z of size 5×5 around a center point $\alpha'_n[x,y]$ in image α'_n.

The median filter estimates the intensity of a pixel surrounded by 8-neighbors of $\alpha'_n[x,y]$ and maps the corresponding pixel's value $\alpha''_n[x,y]$ in the output image α''_n. Median smoothing does not calculate unrealistic intensities for the output image and removes speckle noise from

the angiogram without downgrading arteries' edges. Next, equations (5) and (6) calculate binary mask α''_b by thresholding the denoised image α''_n to zero at the mean grayscale value α''_{mean} of α''_n, as shown in Fig. 3(b).

$$\alpha''_{mean} = \sum_{x=0,y=0}^{x=w-1,y=h-1} \alpha''_n[x,y], (x,y) \in z \quad (5)$$

where z represents the sliding window (5×5) around a center point $\alpha''_n[x,y]$ of image α''_n.

$$\alpha''_b[x,y] = \mu\{\alpha''_n[x,y], \alpha''_{mean}\} \quad (6)$$

where $\alpha''_b[x,y]$ is the resulting pixel intensity at $[x,y]$, μ is the binary thrusholding function, $\alpha''_n[x,y]$ is the input pixel and α''_{mean} is the binary threshold value.

Bitwise subtraction $\ominus$, of image α''_n from its binary mask α''_b generates the required vasculature $\alpha_v = \alpha''_b \ominus \alpha''_n$. Consequently, α_v consists of minimal noise and maximum foreground arterial surface, as shown in Fig. 3(c).

c: BINARIZATION

Having the exact vasculature α_v extracted from the input angiogram α, a thresholding algorithm binarizes α_v into two tones, white and black for background and foreground pixels respectively, without losing essential arterial pixels. To serve our ultimate goal, automatic selection of a single optimal threshold value for binarazation of a diverse range of histogram distributions is not a trivial task. Therefore, instead of global thresholding, an *isodata* or *iterative intermeans* threshold clustering algorithm is employed [17]. Equations (7) and (8) iteratively compute the averages of the background and foreground intensities and calculate an optimal threshold, $\alpha_{iso} = (\alpha_{bg} + \alpha_{fg})/2$.

$$\alpha_{bg} = \left(\sum_{x=0,y=0}^{x=m,y=m} \alpha_v[x,y], (x,y) \in bg\right)/m \quad (7)$$

$$\alpha_{fg} = \left(\sum_{x=0,y=0}^{x=n,y=n} \alpha_v[x,y], (x,y) \in fg\right)/n \quad (8)$$

where bg and fg represent background and foreground surface pixels in α_v respectively, m and n are total number of pixels belonging to relative surface, and α_{bg} and α_{fg} are resultant mean values.

The vasculature image α_v is thus binarized to β and fed into the segmentation process, as shown in Fig. 3(d):

$$\beta\,[x, y] = \begin{cases} 255 \rightarrow \alpha_v[x, y] \geq \alpha_{iso} \\ 0 \rightarrow \alpha_v[x, y] < \alpha_{iso} \end{cases} \quad (9)$$

where $\beta\,[x, y]$ is the resultant pixel at coordinate $[x, y]$ and $\alpha_v[x, y]$ is the input pixel evaluated against the isodata threshold α_{iso}.

2) VASCULAR SEGMENTATION

The type of information necessary for morphological analysis and complexity in the contents of an image determines the criteria for selection of specific segmentation techniques. After applying intensity-based segmentation during pre-processing, the ISADAQ framework employs region-based, edge-based, and component-based segmentation to furnish anatomical and geometrical features for classification. The remainder of this section rationalizes the application of the employed segmentation techniques.
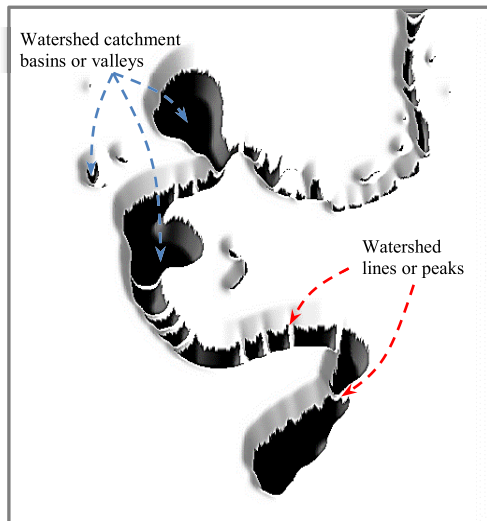

FIGURE 4. 3D Visualization of Watershed Segment.

a: WATERSHED SEGMENTATION

Figure 4 illustrates how a complete arterial surface in binary threshold image β is delineated into several separable segments $\delta_{0...n}$ through *watershed transformation*, based upon anatomical characteristics, as in (10). The transformation algorithm computes valleys or catchment basins from the complex geometry of a given arterial structure and performs region-based segmentation by assigning each pixel of foreground surface to a unique vascular segment (a catchment basin) δ_s in resultant image β_w, as shown in Fig. 5(a).

$$\beta_w = \omega\{\beta(x, y)\} \quad (10)$$

where ω represents watershed segmentation function and β_w is output segmented image.

The simple criterion for assignment of surface pixels of β to non-overlapping segments $\delta_{0...s} = \{\delta_1, \delta_2, \delta_3, \ldots, \delta_s\}$ in β_w is:

$$\delta_{0...s} = \delta_1 \cup \delta_2 \cup \delta_3 \cup, \ldots, \cup \delta_s, \quad \text{and further,}$$
$$\delta_1 \cap \delta_2 \cap \delta_3 \cap, \ldots, \cap \delta_s = 0$$

Watershed segments ($\delta_1, \delta_2, \delta_3, \ldots, \delta_s$) automatically computed and labeled on a binarized angiogram β without manual intervention are on average no less than few dozen. For example, experimental results on the case study image show 63 segments in Fig. 5(a). The size and shape of these segments varies depending upon the complexity of vasculature. The efficiency of segmentation is directly proportional to correct identification of seed points which eventually grow into the regions of similar characteristics. In complex image analysis like brain angiograms the delineation of segments of interest is complicated by the presence of large numbers of indistinct structures like arterial loops, overlapping vessels, and the fact that arteries split and merge. But aneurysmal segments (true-positives) in an angiogram are always delimited accurately through watershed transformation due to clustering of homogeneous pixel intensities around ridges.

The segmentation algorithm superimposes β_w on the extracted vessels structure α_v, to crop out the resultant ROIs from $\mathbb{W}$ for extraction and classification of textural features:

$$\mathbb{W} = (\beta_w \odot \alpha_v) \quad (11)$$

where $\odot$ represents bitwise *AND*, and $\mathbb{W}$ is output of $\odot$ (superimposing β_w on α_v).

Still there is an imperative need to filter out a number of suspect ROIs not only to save overall processing overhead but more importantly to increase the probability of accurate classifications of true positives. Unlike manual approaches of rejecting malignant arterial segments (false-positive), the algorithm seeds automatically calculated points of interest (POIs) into $\mathbb{W}$ so as to sieve a very limited number of watershed segments from $\delta_{0...s}$ as suspected regions of interest (ROIs), as shown in Fig. 5(d).

b: DISTANCE TRANSFORMATION

Most of the existing algorithms for identification of POIs involve manual selection of the seed points which is not only time consuming, but also error-prone if sufficient domain expertise is not available [24]. Therefore, we propose an efficient technique which simultaneously addresses the inherent complexity of arterial structure and also automates the process of calculating POIs. To help with this, the vascular structure in binarized image β is first *distance transformed*, as shown in Fig. 5(b), into β_d by calculating weighted distances from each surface pixel to its closest nonzero boundary pixel:

$$\beta_d\,[x, y] = \mathfrak{X}\{\beta[x, y]\} \quad (12)$$
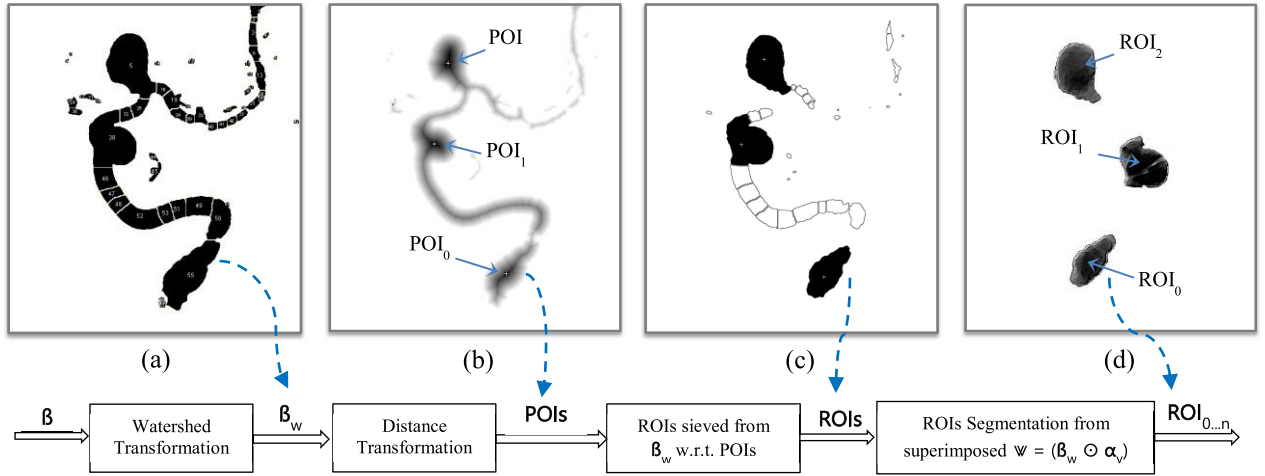
FIGURE 5. Points of Interest (POIs) Calculation and Regions of Interest (ROIs) Segmentation.

where $\mathfrak{X}$ represents the distance transformation function and $\beta_d[x, y]$ is the resultant pixel intensity determined after weighted distance calculation of input pixel $\beta[x, y]$.

The output of distance transformation is an image similar to an artery's topology but the intensities are recalculated according to their weighted distance illustrated in Fig. 5(b). The segmentation algorithm further calculates local maxima on resultant image β_d, which yields $POI_{0...n}$ pointing to locally stable regions:

$$POI_{0...n} = \mathfrak{\mu}\{\beta_d[x, y]\} \tag{13}$$

where $\mathfrak{\mu}$ is the function that calculates $POI_{0...n}$ as local maxima on β_d.

Equation (14) maps the $POI_{0...n}$ calculated in distance transformation to previously identified watershed segments, hence a limited number of suspected $ROI_{0...n}$ are screened out to be classified through trained artificial neural network.

$$ROI_{0...n} = \varkappa\{\mathbb{W}, POI_{0...n}\} \tag{14}$$

where $\varkappa$ is a sieving function that takes $POI_{0...n}$ as input and delineates corresponding $ROI_{0...n}$ from $\mathbb{W}$.

For the experimental results shown in Fig. 5(d), only 3 out of 63 ROIs are sieved as $ROI_{0...2}$ pointed by $POI_{0...2}$. Our automated screening process efficiently reduces the number of candidate true positives earlier in the phase of segmentation, hence aiding the probability of accurate classifications of suspected ROI.

c: UNSHARP MASKING
We experimented with several edge detection techniques to detect the outlines of arterial structures, for example, Canny and Sobel operators, or adaptive and global thresholding etc. [34]. Most of these techniques didn't perform effectively: Canny or Sobel like edge detectors require case-specific threshold values and pre-processing operations for optimal results, and adaptive or global thresholding enhances

unwanted localized details which leads to spurious measurements. By contrast, the unsharp masking filter produces an accurate edge-enhanced image β_m from the input binary threshold image β by subtracting an unsharp (smoothed) version of β from original image β, as in (15). The resultant image β_m, shown in Fig. 6(a), preserves the topological characteristics of the original image β while precisely segmenting the boundary lines of large and small vessels in the angiogram.

$$\beta_m(x, y) = \beta(x, y) \ominus \beta_{smooth}(x, y) \tag{15}$$

where $\ominus$ represents the bitwise subtraction function, β_m is the filtered outline, and β_{smooth} is the blurred version of β acquired through median smoothing operation.

d: SKELETONIZATION
Once the boundary lines have been identified, the segmentation algorithm determines the centerlines of arteries through topological skeletonization, as in (16). During this process, the foreground arterial surface is reduced down to a skeleton (max. 1 pixel wide) while keeping the length and topology of vasculature intact. As compared to morphological thinning, our proposed skeletonization preserves irregularities and other characteristics of tubular and saccular structure inherent to brain arteries and aneurysms, as shown in Fig. 6(b).

$$\beta_s(x, y) = \cup_{r>0} \cap_{q>0} [(\beta \theta \mathrm{r}\beta) - (I\theta \mathrm{r}\beta) \odot \mathrm{q}\beta'] \tag{16}$$

where β_s is the output skeletal image; θ and $\odot$ are the morphological erosion and opening, respectively; $\mathrm{r}\beta$ is an open ball of radius r; and β' is the closure of β.

Each skeletal pixel in β_s is scanned through connected component analysis and is assigned to a unique centerline segment l_s, as shown in Fig. 6(c).

$$\beta_s = l_1 \cup l_2 \cup l_3 \cup \ldots \cup l_s, \text{ and further,}$$
$$l_1 \cap l_2 \cap l_3 \cap \ldots \cap l_s = 0$$
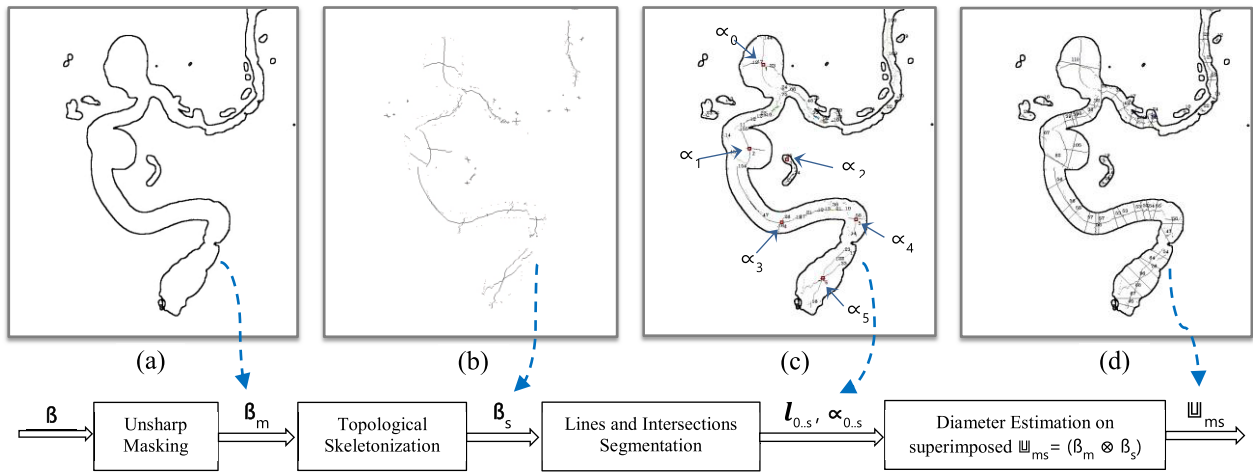
FIGURE 6. Arteries Outlines and Centerlines Detection for Diameter Estimation.

where β_s is skeletal image and $l_{0\ldots s} = l_1, l_2, l_3, \ldots, l_s$ are distinct line segments.

These line segments are further used for geometrical calculations in estimating an aneurysm's rupture score. Similarly, the segmentation algorithm detects line intersections by scanning pixels' neighborhoods in skeletal image β_s. Connected components are analyzed to segment out unique points of intersection $\propto_{0\ldots s}$ in β_s, as depicted in Fig. 6(c), where atleast four lines interconnect. Then the lengths of individual legs of an intersection and the angles between each pair of legs are computed to cross-validate the spherical shape of an aneurysmal segment. Fig. 6(d) shows the skeletal image β_s superimposed on the outline image β_m resulting in U_{ms}, that combines both outline and centerline pixels for calculation and segmentation of arteries based upon their average diameters:

$$\text{U}_{ms}(x, y) = \beta_m(x, y) \otimes \beta_s(x, y) \qquad (17)$$

where U_{ms} is the resultant image, and $\otimes$ is the bitwise *XOR* operation that combines both edges and centerlines of β_m and β_s.

Our algorithm segments out line intersections (with four or more legs merging at a single point) and records them for three purposes; *i)* to cross-validate the classified aneurysm segment η, if its skeleton forms an intersection or not, *ii)* to determine the centroid $\mathbb{C}_{xy}$ of aneurysm surface area for precise geometrical and hemodynamic measurements, and *iii)* to map the centroid $\mathbb{C}_{xy}$ to a specific watershed segment in $ROI_{0\ldots n}$ for respective spatial measurements.

3) ANEURYSM CLASSIFICATION

Machine-based delineation of aneurysms in digital image modalities is challenging due to inter- and intra-clinician variability found in contouring diseased image segments. Therefore, automatic recognition of saccular aneurysms requires the classifier to be trained upon significant visual features of regions of interest (ROIs) which may correctly classify different arterial segments. For this purpose, spatial relationship among gray level pixel intensities of candidate ROIs has been observed to exhibit exclusive pixel arrangements which can be used to distinguish surface areas of saccular aneurysms from non-aneurysms. Such distinctive textural characteristics are computed as 1st-order (e.g. histogram features), 2nd-order (e.g. Gray-Level Co-occurrence Matrix – GLCM or Gray-Tone Dependency Matrix - GTDM) and higher-order (e.g. Gray-Level Run Length Matrix – GLRLM) statistical data.

To best of our knowledge, the intrinsic ability of textural features to correctly classify aneurysmal segments, not only with higher accuracy but also at lower computational cost, has never been exploited for digital subtraction angiography (DSA) image categorization. However, texture analysis has been widely used since its conception [18], [20] in comparison to other optical, fractal and modal-based techniques for medical image segmentation, detection, classification and compression tasks. More specifically, a set of fourteen 2nd-order statistical correlations between neighboring pixel intensities in a given textured segment (named *Haralick* features) presented in Table-1 are known as one of the most significant descriptors for classification of multispectral medical images like angiograms [25]. These descriptors are of primary interest to our classification technique because they collect discrete grayscale tonal primitives of candidate ROIs by computing image signal statistics in the spatial domain. For instance, fineness, coarseness, smoothness, randomness, granulation, and lineation are some of the distinguishable visual characteristics which are locally consistent among boundary and surface intensities of aneurysmal and non-aneurysmal regions.

The classification algorithm extracts *Haralick* features as spatial distribution of tonal variations among gray shades in the histogram of each ROI segment. This unique feature vector inherently represents substantive structural arrangement between foreground and background surface pixels of

TABLE 1. Haralick textural features and their mathematical definitions.

	Features	Definition
f_1	Angular Second Moment *or* Homogeneity	$\sum_i \sum_j \{p(i,j)\}^2$
f_2	Contrast	$\sum_{n=0}^{L-1} n^2 \{\sum_{i=1}^{L} \sum_{j=1}^{L} p(i,j)\}$ $\qquad\quad |_{\,i-j=1\,|}$
f_3	Correlation	$\{\sum_i \sum_j (ij)p(i,j) - \mu_x \mu_y\}/\sigma_x \sigma_y$ where μ_x and μ_y are the means and standard deviations of p_x and p_y
f_4	Sum of Squares: Invariance	$\sum_i \sum_j (i-\mu)^2 p(i,j)$
f_5	Inverse Difference Moment	$\sum_i \sum_j \frac{1}{1+(i-j)^2} p(i,j)$
f_6	Sum Average	$\sum_{i=2}^{2L} i p_{x+y}(i)$
f_7	Sum Variance	$\sum_{i=2}^{2L} (i - f_8)^2 p_{x+y}(i)$
f_8	Sum Entropy	$-\sum_{i=2}^{2L} p_{x+y}(i) \log\{p_{x+y}(i)\}$
f_9	Entropy	$-\sum_i \sum_j p(i,j) \log\{p(i,j)\}$
f_{10}	Difference Variance	*variance of* p_{x-y}
f_{11}	Difference Entropy	$-\sum_{i=0}^{L-1} p_{x-y}(i) \log\{p_{x-y}(i)\}$
f_{12} f_{13}	Info. Measure of Correlation 1,2	$\dfrac{HXY - HXY1}{\max\{HX, HY\}}$ $(1 - \exp[-2.0(HXY2 - HXY)])^{1/2}$ and $HXY = -\sum_i \sum_j p(i,j) \log\{p(i,j)\}$ where HX and HY are entropies of p_x and p_y, and $HXY1 = -\sum_i \sum_j p(i,j) \log\{p_x(i)p_y(j)\}$ $HXY2 = -\sum_i \sum_j p_x(i)p_y(j) \log\{p_x(i)p_y(j)\}$
f_{14}	Maximal Correlation Coefficient	$(second\ largest\ eigenvalue\ of\ Q)^{1/2}$ where, $Q(i,j) = \sum_k \frac{p(i,k)p(j,k)}{p_x(i)p_y(k)}$

every ROI segment [22]. Each feature vector is further annotated as 'aneurysmic' or 'non-aneurysmic' with the help of domain experts for training purposes. The labeled features set is input to train and test accuracy of different classifiers for cross validation, including Multilayer Perceptron (MLP) neural network, Support Vector Machine (SVM), etc. Based upon the optimum performance, as compared to other statistical classifiers, our framework classifies ROIs using a feed-forward back-propagation MLP neural network, as explained in the following section.

a: HARALICK FEATURE VECTOR

Spatial dependencies and inter-pixel relationships defined by second order statistical matrices calculated through GLCM [19] are used to extract fourteen *Haralick* texture features [20], defined in Table-1, which characterize the unique arrangement of gray-level transitions exiting in an image segment. These statistical measures are computed for each of the automatically segmented $ROI_{0...n}$ from four gray-level co-occurrence matrices calculated in different directions of adjacency, $\theta = 0°, 45°, 90°$, and $135°$. For example, the *Contrast* feature is the measure of intensity contrast between a pixel and its neighborhood. If the gray scale difference occurs continually, the texture becomes coarse and the

contrast becomes large; otherwise, the texture becomes acute if the contrast has a small value. Similarly, *Correlation* measures how correlated a pixel is to its neighborhood, i.e. the measure of gray tone linear dependencies in an image segment. Its values range from -1 to 1, which indicate perfect negative and positive correlation, respectively. Consequently, a single feature vector comprising 56 (14×4) numerical values describing the semantics of a textured region possesses salient capabilities to encode correlating local neighborhood intensities of a candidate ROI which is input to train a specific classifier.

Analyzing these tonal variations between angiogram image segments, a machine classifier can approximate unknown correlations between input feature vectors and corresponding output classes, hence correctly distinguish an aneurysmal region from non-aneurysmal regions of interest. Lastly, a successfully recognized aneurysmal segment η is deferred to the estimation algorithm to precisely calculate its geometrical characteristics and to quantify its rupture score.

b: FEATURE CLASSIFIERS

The *Haralick* feature vectors computed through GLCM [19] are labeled with the help of a domain expert and exhaustively tested using cross validation. In order to achieve optimal results from a machine classifier, certain choices are imperative pertinent to ROI characterization of ISADAQ: *a)* ROI dimensions and color space selection, and *b)* features set and classifier selection. Hence, each ROI segment is automatically resized to a 100 x 100 grayscale image prior to training and testing, and features set comprising of 2nd order spatial correlations are calculated from GLCM. We chose the Multi-layer Perceptron (MLP) neural network, based upon its ability to recognize the tonal semantics of saccular aneurysm segments with highest accuracy as compared to well-known statistical classifiers including Support Vector Machine, Logistic Regression and Naïve Bayes. The results of a comparative study of multiple classifiers trained upon Haralick textural features is presented in *Section-IV*.

c: MULTILAYER PERCEPTRON (MLP) NEURAL NETWORK

Artificial neural networks have recently become a dominant technique for learning and recognizing complex data patterns. Among its different architectures, Multilayer Perceptron (MLP) neural network [12] is considered the most assertive supervised neural network topology which is capable of classifying non-linearly separable data sets through a gradient-descent learning algorithm called backpropagation. An MLP network comprising of at-least three layers (*input* – first layer, *hidden* – one or more layers, and *output* – last layer) and an arbitrary number of processing elements (called *sigmoidal nodes*) in each layer can be efficaciously used to characterize ROIs textural features. We used a four-phase training cycle as described below, in which the activation nodes identify repeating patterns from statistical features and continuously generalize network performance by adapting new data patterns in successive learning cycles.
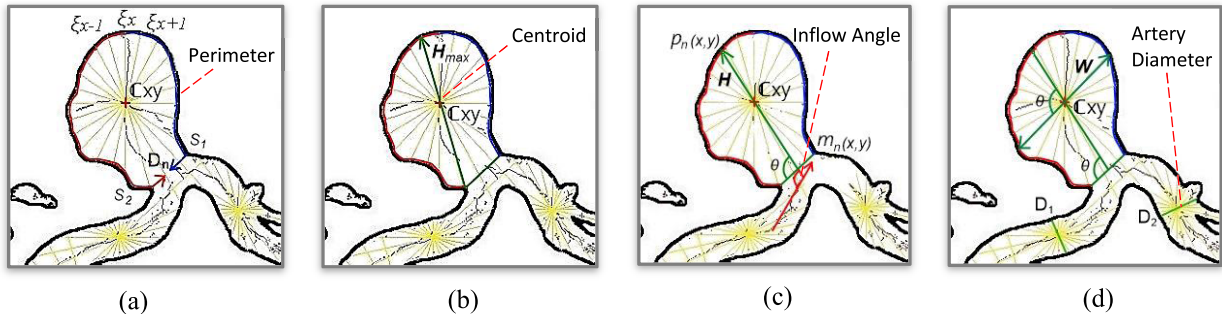
FIGURE 7. Aneurysm's local geometrical features; (a) neck diameter D_n, (b) maximum height H_{max}, (c) height H, (d) width W.

I   Configuring the network of required number of layers and perceptrons ($\rho_1, \rho_2, \rho_3, \ldots, \rho_n$), and initializing the links between pairs of nodes in adjacent layers with random synaptic weights (w_{ij}), i.e. small numbers between -1.0 and 1.0, defining the strengths of each connection.

II Providing the input features $f_{1,0^o}, f_{2,0^o}, f_{3,0^o}, \ldots,$ $f_{14,135^o}$ to input layer nodes $I_1, I_2, I_3, \ldots, I_{56}$, so that non-linear inner products of each node ρ_i can be calculated and fed forward to the succeeding perceptron ρ_j using a sigmoid activation function $\sigma_j = 1/(1 + e^{-\rho_j})$, where $\sigma_j = \sum_{i=1}^{n} w_{ij} f_i$ is weighted sum of input features.

III Computing the magnitude of error ∂_i of output units O_1, O_2, as, $\partial_i = t_i - \sigma_i$, by comparing their calculated activations with the target activation and propagating it back through all hidden layer units with respective mean square errors cumulated as, $\partial_i = \sigma_i \sum_{j}^{m} w_{ij} \partial_j$.

IV Recalculating the initial synaptic weight w_{ij} of each link between locally connected pairs of processing nodes ρ_i and ρ_j by adding the change Δw_{ij}, calculated as, $\Delta w_{ij} = \tau \partial_j \delta \sigma_i$, where ∂_j is the mean square error, δ is small learning rate and τ is the momentum term, taken as 0.3 and 0.2 respectively to achieve maximum accuracy out of experimental network.

4) RUPTURE RISK QUANTIFICATION

The heart of ISADAQ is a geometrical assessment of an accurately classified saccular brain aneurysm η for computing its rupture score on the basis of local and spatial characteristics. The proposed estimation algorithm quantifies geometrical features namely: neck diameter (D_n), maximum height (H_{max}), aneurysm height perpendicular to neck diameter (H), maximum width (W) and average diameter of connecting artery (D_{avg}), as depicted in Fig. 7(a, b, c, d). Then based upon these attributes, ISADAQ calculates a BASSH (*Bottleneck factor, Aspect ratio, Size ratio, Surface area, Hemodynamic factor*) Score to predict the rate of rupture as follows:

  i   Bottleneck Factor (μ) $= W/D_n$
  ii Aspect Ratio (λ) $= H/D_n$
  iii Size Ratio (δ) $= H_{max}/D_{avg}$

  iv Surface Area (Ω) $= W \times H$
  v   Hemodynamic Factor ($\mathfrak{h}$) $= \varrho \times \theta \times c$

Note that the proposed algorithm calculates these ratios in pixels. Although translating pixels into millimeters could increase the radiologist's understanding, due to the diverse range of image resolutions and contents, the scale can't be generalized. Likewise, the geometrical ratios between scaler attributes waive the need of such calibration because their correlations correspondingly reflect the risk associated with calculated sizes.

To promote greater accuracy and precision in calculation of basic and derived parameters, we have observed the following conditions:

- Aneurysm centroid $\mathbb{C}_{xy}$ should be identified before calculating W, H and H_{max}
- Line segments computing W, H and H_{max} should pass through $\mathbb{C}_{xy}$
- Blood inflow angle is the angle between the axis of the parent artery with respect to the direction of aneurysm H
- Aneurysm maximum width W should be calculated parallel to D_n
- D_{avg} should be average of contiguous arteries to aneurysm

a: GEOMETRICAL FEATURES ESTIMATION

Our estimation technique draws several lines on $\mathbb{U}_{ms}$ passing through aneurysm centroid $\mathbb{C}_{xy}$ towards boundaries on both sides by rotating the wheel at the angle of φ degrees. For example, Fig. 7(a) shows the rotation of wheel at φ (e.g. 15 degrees) and both the edges of diameters touching the boundary lines are recorded for perimeter estimation, hence resulting a list of edges $\xi_{1..24}(360/\varphi)$. The proposed algorithm runs two snakes S_1 and S_2, scanning internal boundary of an aneurysm in opposite directions from an edge ξ_x, towards ξ_{x+1} and ξ_{x-1}. At any two points P_i and P_j for S_1 and S_2 respectively, snakes search for M x M pixels in their neighborhoods to find the locations that minimize the energy function and move P_i and P_j to that location, until $P_i = P_j$. For an aneurysm with an open neck towards the connecting artery, the perimeter can only be defined after the neck diameter D_n is identified.

1) NECK DIAMETER (D_n)

The proposed algorithm scans every pixel from one edge to another and computes the average distance between adjacent edges while adding the pixels to the resultant perimeter vector $\mathbb{P}$, as presented in Fig. 7(a). Each of the pixels $p_i(x, y)$ and $p_j(x, y)$ is analyzed with respect to the direction maintained by their previous n pixels towards target edges ξ_i and ξ_j, respectively. An aneurysm neck is identified where there is no direct adjacent pixel in the $M \times M$ neighborhood in the direction of target edge ξ_i or ξ_j. Those points where pixels began to are recorded as $D_i(x, y)$ and $D_j(x, y)$ and S_1 and S_2 scans the next n pixels with connectivity. If the divergence continues increasing for the next n pixels, then the shortest distance between $D_i(x, y)$ and $D_j(x, y)$ is calculated as the neck diameter D_n and the last n pixels are discarded.

ii) ANEURYSM MAXIMUM HEIGHT (H_{max})

Fig. 7(b) shows that several lines from each point $d_n(x, y)$ on D_n are drawn, passing through $\mathbb{C}_{xy}$ towards a point $p_n(x, y)$ on $\mathbb{P}$ and the longest distance from $d_n(x, y)$ to $p_n(x, y)$ is recorded as an aneurysm's maximum height H_{max}.

iii) ANEURYSM HEIGHT (H)

As shown in Fig. 7(c), the algorithm determines the midpoint $m_n(x, y)$ on D_n and draws a line on $m_n(x, y)$ that passes through $\mathbb{C}_{xy}$ and touches $\mathbb{P}$ at $p_n(x, y)$. The distance between two points $m_n(x, y)$ and $p_n(x, y)$ is recorded as aneurysm height H.

iv) ANEURYSM WIDTH (W)

The angle θ of H on D_n is determined, as shown in Fig. 7(d), and the aneurysm diameter W is calculated with same angle θ on H at $\mathbb{C}_{xy}$.

v) ARTERY AVERAGE DIAMETER(D_{avg}) An artery's diameter is estimated by calculating the shortest distance D_s from the centerline l_s towards the boundaries of the artery in $\mathbb{U}_{ms}$. Several diameters $D_{0...s}$, from one edge to the other of the respective artery are drawn passing through specific points on each line segment l_s in $l_{1..s}$. As shown in Fig. 7(d), D_1 and D_2 are diameters of two arteries calculated as, *i*) from the list of watershed segments $\delta_{0...s}$, connecting arteries and their respective midlines are identified as $l_{1,2}$, *ii*) several lines are drawn passing through the mid points of $l_{1,2}$, *iii*) end point of l_s, and any point of intersection $\propto_s$ in $\propto_{0...s}$. Lastly, from the list of watershed segments $\delta_{0...s}$, connecting arteries and their respective skeletal are identified and their average diameter is estimated as D_{avg}.

b: ANATOMICAL FACTORS ESTIMATION

i) BOTTLENECK FACTOR *(μ)*

Among shape indices of saccular aneurysm, μ has been recorded as a critical factor in prediction of aneurysm rupture [11], [13], [17]. Defined as, W/D_n, higher values of μ mean that the neck diameter is relatively much smaller than the aneurysm's maximum width. This increases the probability of rupture because of the high wall shear stress caused by abnormal blood flow into the aneurysmal sac.

ii) ASPECT RATIO (λ)

Another important factor in determining the rupture probability of an aneurysm is the ratio between the height and diameter of its neck, i.e. H/D_n [19], [23], [30]. Medical analysis of historical data demonstrates that if the neck size of a saccular aneurysm is smaller than the height of aneurysm dome, the probability of rupture is higher. So higher values of λ, increase the risk of aneurysmal rupture.

iii) SIZE RATIO (δ)

The maximum height of the aneurysm dome with respect to the diameter of the connecting artery has been proven to be the most significant size index in prediction of saccular aneurysm rupture [12], [21], [22]. Temporal analysis of saccular aneurysms suggests that higher values of $\delta = H_{max}/D_{avg}$, increase the probability of rupture and categorizes it as either dangerous or safe.

iv) SURFACE AREA (Ω)

Another observable factor in predicting the rate of rupture of an aneurysm is Ω [11], [27], [39], that is determined as area covered by total width multiplied by total height of an aneurysm sac, i.e. WxH. Surface area helps in categorizing saccular aneurysms among different sizes suggested in previous clinical studies [15], [17], [35] (extra-small, small, medium, large, extra-large, and giant). Following are the ranges in pixels and respective measurements in *mm* according to (18) to determine aneurysm size factor (Ω_w) as defined below:

$$1mm \approx 3.78px$$
$$\therefore (1 \times 1)\, mm^2 \approx (3.78 \times 3.78)px^2$$
$$\therefore 1mm^2 \approx 14.29px^2 \tag{18}$$

a. X-Small ($<= 1.99mm^2$) $=< 28px^2$ ($\Omega_0 = 0$)
b. Small (2.0–$4.9mm^2$) $= 29$–$70px^2$ ($\Omega_1 = 1$)
c. Medium (5.0–$9.9mm^2$) $= 71$–$141px^2$ ($\Omega_2 = 2$)
d. Large (10.0–$14.9mm^2$) $= 142$–$213px^2$ ($\Omega_3 = 3$)
e. X-Large (15.0–$24.9mm^2$) $= 214$–$356px^2$ ($\Omega_4 = 4$)
f. Giant ($>= 25mm^2$) $=> 357px^2$ ($\Omega_5 = 5$)

v) HEMODYNAMIC FACTOR (ʄ)

Another important factor mainly affecting the quick growth of saccular aneurysm size is the angle of blood flowing into the aneurysm sac from the parent artery [6], [31], [32], [40], calculated as θ as shown in Fig. 7(c). A detailed literature review of morphological analyses of neuroimaging shows that hemodynamic flow patterns (aneurysm location with respect to the direction of blood flow in the parent artery) has never been suggested for aneurysmal rupture estimation.

TABLE 2. POIs calculated for angiogram images, showing %age of POIs reduced after Distance Transformation.

#	1	2	3	4	5	6	7	8	9	10	11	12
$POI_{0..m}$	38	39	41	36	12	58	13	60	144	27	23	38
$POI_{0..n}$	4	6	2	9	3	3	5	2	6	7	4	2
$POI_{0..s}$	34	33	39	27	9	55	8	58	138	20	19	36
%	89	84	95	75	75	95	61	97	96	74	83	95

(a)   (b)
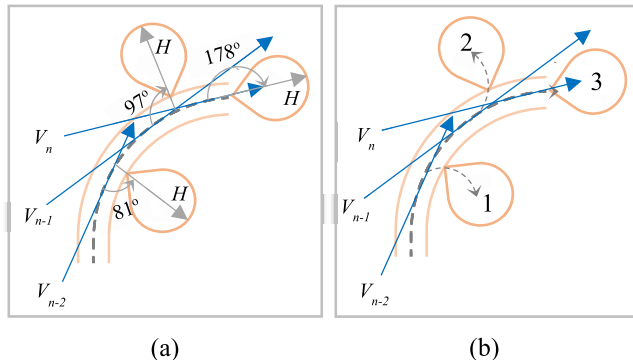
FIGURE 8. (a) Determining inflow angle at intersection of vector *H* and artery midline vector *V*, (b) Determining inflow rupture factor (1,2,3) using blood flow direction approximated through midline of connecting artery.

As depicted in Fig. 8, a saccular aneurysm can be located inward, outward or in-line with respect to the parent vessel. The aneurysm's location causes different stress levels (defined as, stress factor) on the aneurysm walls respectively, defined as, $\varrho = 1$ (minimum), $\varrho = 2$ (moderate), and $\varrho = 3$ (maximum). Our algorithm first determines the proximal direction of the parent artery by drawing vectors $V_{1..n}$ using the artery's midline and locate the aneurysm centroid with respect to that, then calculates the blood inflow angle by extending the vector H from the centroid toward the aneurysm neck and calculates angle θ by intersecting the connecting midline vector. Finally, the tendency of blood inflow into saccular aneurysm is calculated as, $\mathfrak{h} = \varrho \times \theta \times c$, where c = 0.01, is a constant defined for normalizing rupture score.

c: BASSH SCORE ESTIMATION

The probability of aneurysm rupture is estimated by first determining the size factor (Ω_w) as described earlier. Then individual weights are assigned (between 0.0 – 1.0) with the help of expert neurosurgeons based upon degrees of risk involved with individual anatomical factors (such as: w_μ– bottleneck factor, w_λ – aspect ratio, w_δ – size ratio, w_Ω – surface area, $w_\mathfrak{h}$ – hemodynamic factor). Finally, the risk of rupture is quantified as the BASSH score (ε) by taking the sum of products of risk factors with their respective weights as shown below:

$$\varepsilon = w_\mu \times \mu + w_\lambda \times \lambda + w_\delta \times \delta + w_\Omega \times \Omega_w + w_\mathfrak{h} \times \mathfrak{h} \quad (19)$$

TABLE 3. Unruptured intracranial aneurysm severity index (IASI).

ε	0.0–0.9	1.0–1.9	2.0–2.9	3.0–3.9	4.0+
IASI	Safe	Mild	Moderate	Severe	Critical

TABLE 4. MLP Neural Network classification results w.r.t. # of hidden layers.

#	Accuracy	Sensitivity	Specificity	Precision	Recall
1	78 %	0.83	0.77	0.81	0.78
2	84 %	0.74	0.88	0.84	0.88
3	95 %	0.91	0.97	0.95	0.95
4	95 %	0.91	0.97	0.95	0.95
5	94 %	0.91	0.96	0.94	0.94
6	98 %	0.97	0.99	0.98	0.98
7	97 %	0.97	0.97	0.97	0.97
8	97 %	0.97	0.97	0.97	0.97
9	97 %	1.00	0.96	0.97	0.97
10	97 %	0.97	0.97	0.97	0.97

In consultation with a senior neurosurgeon, the following weights were assigned and further evaluated to achieve the closest possible accuracy with respect to ground truth: $w_\mu = 0.05$, $w_\lambda = 0.1$, $w_\Omega = 0.4$, $w_\delta = 0.4$, and $w_\mathfrak{h} = 0.05$.

The lower the BASSH score (ε), the safer a patient is, and the higher the BASSH score is, the higher the risk of rupture. The BASSH score is mapped and validated against the unruptured Intracranial Aneurysm Severity Index (IASI) defined with help of expert neurosurgeons, as shown below.

IV. RESULTS AND EVALUATION

For implementation and performance evaluation of ISADAQ, we used open source and proprietary tools including OpenCV [33] for image pre-processing tasks, ImageJ [34] for image segmentation, Weka [35] for MLP neural network and statistical classification, and Microsoft Accord.NET [36], [37] for Haralick feature extraction and BASSH score estimation.
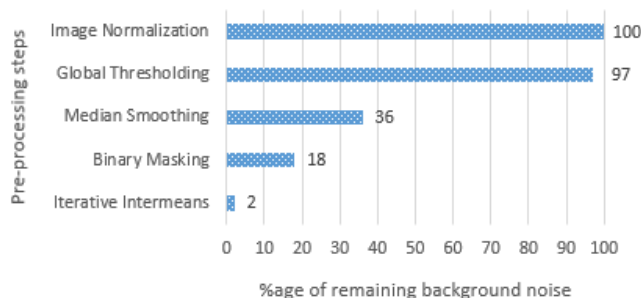
A. EFFECTIVENESS OF ANGIOGRAM PRE-PROCESSING

The purpose of this evaluation is to validate the approach we took for the pre-processing of Digital Subtraction Angiograms (DSA). Since bulged-out areas in angiograms are more likely to be aneurysms, geometrically they span over

TABLE 5. MLPNN classification accuracy (in %age) with 0th, 1st, 2nd, and 3rd –order texture statistics computed for original and noisy ROIs.

ROIs	Original				Poisson Noise				Gaussian Noise			
Naïve Bayes	69.52	50.47	49.04	77.14	68.57	54.28	46.19	61.9	73.33	45.71	46.19	64.76
SVM	83.8	66.66	66.38	77.14	68.57	66.66	63.33	62.85	74.28	63.8	63.33	60
Logistic Regression	81.9	59.04	92.19	73.33	70.47	76.19	84.76	60.95	75.23	68.57	79.04	60.95
MLPNN	84.76	82.85	98.09	74.28	80.95	80.95	96.19	57.14	81.9	80	95.23	64.76
Order	0th	1st	2nd	3rd	0th	1st	2nd	3rd	0th	1st	2nd	3rd

a larger spatial area forming a spherical region. In manual diagnosis, the phase contrast material used in angiography is the key to pinpoint such suspected regions of vascular pathology, so we exposed similar characteristics from the input angiogram during pre-processing to improve the accuracy of the subsequent segmentation process. ISADAQ reduces a substantial amount of background noise from the angiogram at each step from image normalization through binarization using different morphological operations. Figure-9 presents average results of 59 angiograms showing how the global thresholding process denoises normalized angiograms up to 3%, median smoothing reduces background noise to 64%, binary masking further cuts it down to 18% and finally iterative intermeans leaves the image in binarized form with at most 2% background noise, and maximum foreground surface pixels which represent vascular structure to be segmented further.

**FIGURE 9.** Background noise reduced through pre-processing steps.

B. EFFECTIVENESS OF VASCULAR SEGMENTATION

Most previously proposed segmentation techniques are limited by the need to manually provide seed points to delimit pre-processed brain images into candidate ROIs using region growing approaches. ISADAQ's segmentation algorithm, on the other hand, efficiently automates angiogram image segmentation by identifying stable points of maximum intensities. These regions of higher local intensities in angiograms represent the presence of dye material injected during Digital Subtraction Angiography, which stays in brain arteries for certain amount of time. We calculate a very limited number of such *local maxima* as points of interest (POIs) from the *Distance Transformed* image as shown in Fig. 5(b), instead of pre-processed angiogram, and seed them into *Watershed Segmented* regions of interest (ROIs).

TABLE 6. MLPNN efficiency in terms of accuracy at minimal cost (time/space)

	Accuracy (%)	Time (sec)	Space (min. layers)
0th Order	84.76	1.39	4 (with PCA)
1st Order	82.85	1.13	10
2nd Order	98.09	1.36	6
3rd Order	74.28	1.91	2 (with PCA)

Table-2 validates the significance of calculating $POI_{0...n}$ after applying distance transformation on binarized angiograms as compared to the large number of $POI_{0...m}$ calculated from the pre-processed image before binarization. Therefore, discarding a significant number of $POI_{0...s}$, as recorded in Table-2, is the key to enhance the efficiency of our segmentation technique because $POI_{0...n}$ are used to pinpoint a very limited number of segmented $ROI_{0...n}$, which ultimately improves the performance of the machine classifier. The evaluation results presented in Table-2 show that we could eliminate almost 80-90% of false positive and false negative ROIs through the sieving process described above, while ensuring that saccular aneurysm segments, if they exist in an angiogram, are always signified by at-least one of the POIs in $POI_{0...n}$.
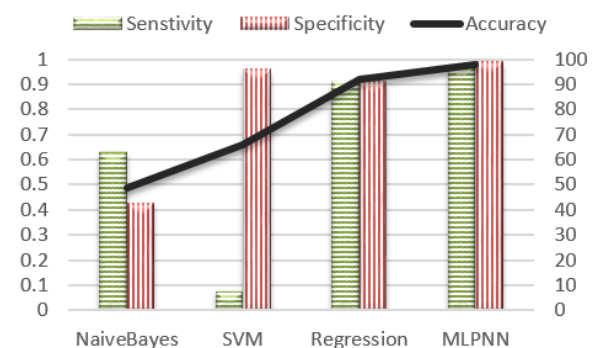
FIGURE 10. ROI classification performance.

C. EFFECTIVENESS OF ANEURYSM CLASSIFICATION

Figure-10 shows the comparative results of ROI classification in terms of highest accuracy (98%), sensitivity (0.97) and specificity (0.99) achieved by the Multilayer Perceptron (MLP) Neural Network as compared to other statistical classifiers including, Naïve Bayes with minimum accuracy (49%), Support Vector Machine (SVM) with relatively improved accuracy (66%), and Logistic Regression (92%). In order

TABLE 7. Geometrical attributes and BASSH Score calculation (ε) for randomly selected angiograms.

#	D_n (px)	H (px)	W (px)	H_{max} (px)	D_{avg} (px)	B μ	A λ	S δ	S Ω_W	H ƒ	Score ε	εi	εx
1	39	74	75	86	29	1.92	1.9	2.97	5	0.72	3.51	Severe	Severe
2	35	54	43	50	13	1.23	1.54	3.85	3	4.08	3.16	Severe	Severe
3	16	64	54	78	20	3.38	4	3.9	4	1.14	3.79	Severe	Critical
4	44	61	51	68	33	1.16	1.39	2.06	4	1.96	2.72	Moderate	Moderate
5	28	148	116	158	20	4.14	5.29	7.9	5	2.26	6.01	Critical	Critical
6	32	74	66	88	21	2.06	2.31	4.19	4	0.84	3.65	Severe	Severe
7	48	38	60	59	14	1.25	0.79	4.21	3	1.84	3.12	Severe	Severe
8	29	48	61	53	19	2.1	1.66	2.79	3	5.16	2.85	Moderate	Severe
9	57	113	104	116	37	1.82	1.98	3.14	5	1.08	3.60	Severe	Critical
10	36	88	66	101	35	1.83	2.44	2.89	5	3.99	3.69	Severe	Severe
11	91	89	84	108	73	0.92	0.98	1.48	5	1.8	2.83	Moderate	Moderate
12	63	94	119	106	48	1.89	1.49	2.21	5	1.53	3.20	Severe	Moderate

to train and test different machine classifiers, we prepared a dataset of 210 ROIs, automatically segmented out from 59 angiograms, and manually labeled with expert input as *aneurysmic* or *non-aneurysmic*. The experimental configuration for outperforming MLP comprises of 56 input nodes (i.e. 14-Haralick features x 4-adjacency angles), 2 output nodes (for binary classification – aneurysm or not), 6 hidden layers and 28 perceptrons. This network configuration was exhaustively tested with 10-fold cross validation in order to eliminate the error of bias. We evaluated MLP by altering its configuration and recorded classification results in Table-4. It is observed that although computational complexity increased exponentially with increasing number of hidden layers (from 1 to 10) and activation nodes (from 2 to 28), the classification performance also rose to 98.09%, which stayed nearly consistent after 6 hidden layers containing 28 sigmoid nodes.

We further evaluated the robustness of proposed MLP neural network in terms of consistent accuracy achieved before and after injecting most susceptible noise profiles into training ROIs [49]. For this purpose, we have injected Poisson and Gaussian noise models which have been designated by several studies on medical imaging in the past [46], [48], [50]. Poisson or Quantum noise and Gaussian or Additive noise incisively imitate the random behavior of photons distribution expected in X-rays based fluoroscopic images like DSA. Likewise, subtraction of digital images acquired before and after contrast medium injection also introduce additional noise to the resultant DSA images. Therefore, several techniques including receptor sensitivity adjustment, controlling contrast material quantity and also noise removal algorithms [46], [47] have been proposed to mitigate the noise levels.

In addition to injecting the noise profiles, we extended the scope of our robustness evaluation scheme by computing 0th, 1st, 2nd, and 3rd–order texture features of noisy ROI segments for training MLP neural network. Here, 0th-order texture features represent raw pixel data, and 1st-order features are estimated as mean, variance, skewness, kurtosis, energy, and entropy. Whereas, 2nd and 3rd–order texture features are

computed from Grey-level Co-occurrence Matrix (GLCM) and Gray-level Run-length Matrix (GLRLM), respectively. The classification results of proposed network were compared to the classification results of original ROIs with similar texture features. Table-5 records the results of our rigorous evaluation and validates that feed-forward back-propagation MLP neural network yields highest classification accuracy with 2nd-order texture features, not only for original ROIs but also for noisy ROIs. Our 10-fold cross validation also proves that MLPNN classifies intracranial saccular aneurysms consistently better than other three machine classifiers (Naïve Bayesian, SVM, and Logistic Regression), when trained and tested with variable texture features extracted from ROIs carrying both the noises.

Finally, we evaluated the efficiency of MLPNN in terms of computational and space overhead. We have found the highest accuracy, 98.09%, of proposed neural network with 2nd-order statistical features at the cost of minimum space required by 6 hidden layers and 1.36 seconds for training the model. Shown in Table-6 is the minimum time and space requirements for training MLP neural network on texture features computed at different statistical orders. The results manifest our selection of 2nd-order Haralick features for classification of aneurysmic ROIs with maximum accuracy at optimum cost of time and space. Whereas, 1st-order texture features are rejected due to lower accuracy achieved with highest number of 10 hidden layers. Similarly, 0th and 3rd− order image statistics are ruled out because of additional computational overhead imposed by inevitable requirement of reducing larger feature set to smaller ones using Principal Component Analysis (PCA).

D. EFFECTIVENESS OF RUPTURE RISK QUANTIFICATION

The evaluation of the quantification algorithm is based on successful categorization of aneurysm's BASSH score upon Intracranial Aneurysm Severity Index (IASI) presented in Table-3. Table-7 presents quantification results estimated through an aneurysm's geometrical factors calculated in terms of BASSH score (ε) for 12 randomly selected angiograms out of 47 angiograms overall. Each score

estimated from an individual ROI's local and spatial factors is automatically ranked between 0.0 to 4.0+, as εi shown in Table-7. Finally, the predicted rupture probabilities are validated through expert neurosurgeons and the difference is recorded as εx in Table-7. The quantification results show that 86% of aneurysms were found correctly classified against gold standard whereas 14% were mis-classified either due to error in the geometrical features estimation algorithm (9%) or due to unknown anatomical factors (6%) which contradict the BASSH score formula defined in (19).

V. CONCLUSIONS AND FUTURE DIRECTIONS

Using a case study based approach, this paper presented a fully automated framework (ISADAQ) which performs morphological, anatomical, and textural analysis of brain angiograms (DSA) to accurately identify saccular aneurysms and quantify their rupture probability. The methodology presented in the preceding sections efficiently resolves the most significant research questions through comprehensive investigation of image processing and machine learning techniques. Our selection of angiograms instead of other neuro imaging modalities, e.g., MRA and CTA, for intracranial aneurysm diagnosis was based upon the facts that: i) DSA is still used as the most decisive medium for concluding any clinical treatment for unruptured aneurysms; ii) DSA possesses unique textural characteristics which can be used for efficient recognition of malignant lesions; and iii) DSA provides maximum contrast between cerebral arteries and tissues, allowing precise estimation of size and rupture probability of saccular aneurysms.

Prior studies regarding aneurysm rupture score estimation mostly relied on clinical factors involving maximum manual input whereas we propose BASSH score calculations through morphological analysis of angiograms involving minimum human intervention. ISADAQ's encouraging results are a first and significant step toward our long-term objective of designing a clinical Decision Support System (DSS) that will employ automated detection and quantification for periodic study of aneurysmal growth over the course of a number of aneurysmal subarachnoid hemorrhages (aSAH). This future work may include the following:

- To extend the scope of ISADAQ towards investigating DSA for automated detection and quantification of multiple aneurysms, treated aneurysms, irregular saccular aneurysms, and other forms of intracranial aneurysms, e.g. fusiform, distal, and dissection.
- To improve BASSH score through information fusion of this score with semantic based analysis of clinical data (structured and unstructured one).
- To extend the proposed framework for periodic follow-up study of aneurysmal growth using 2D and 3D brain image modalities.

REFERENCES

[1] *Brain Aneurysm Statistics and Facts*. [Online]. Available: http://www.bafound.org/about-brain-aneurysms/brain-aneurysm-basics/brain-aneurysm-statistics-and-facts/

[2] NINDS. (May 10, 2017). *Cerebral Aneurysms Fact Sheet*. [Online]. Available: https://www.ninds.nih.gov/Disorders/Patient-Caregiver-Education/Fact-Sheets/Cerebral-Aneurysms-Fact-Sheet

[3] D. J. Nieuwkamp, L. E. Setz, A. Algra, F. H. H. Linn, N. K. de Rooij, and G. J. E. Rinkel, "Changes in case fatality of aneurysmal subarachnoid haemorrhage over time, according to age, sex, and region: A meta-analysis," *Lancet Neurol.*, vol. 8, no. 7, pp. 635–642, Jul. 2009, doi: 10.1016/S1474-4422(09)70126-7.

[4] J. Bisbal, G. Engelbrecht, M.-C. Villa-Uriol, and A. F. Frangi, "Prediction of cerebral aneurysm rupture using hemodynamic, morphologic and clinical features: A data mining approach," in *Proc. 22nd Int. Conf. Database Expert Syst. Appl. (DEXA)*, 2011, pp. 59–73, doi: 10.1007/978-3-642-23091-26.

[5] D. Backes *et al.*, "PHASES score for prediction of intracranial aneurysm growth," *Stroke*, vol. 46, no. 5, pp. 1221–1226, 2015, doi: 10.1161/STROKEAHA.114.008198.

[6] S. Siuly and Y. Zhang, "Medical big data: Neurological diseases diagnosis through medical data analysis," *Data Sci. Eng.*, vol. 1, no. 2, pp. 54–64, 2016, doi: 10.1007/s41019-016-0011-3.

[7] M. J. H. Wermer, I. C. van der Schaaf, A. Algra, and G. J. E. Rinkel, "Risk of rupture of unruptured intracranial aneurysms in relation to patient and aneurysm characteristics an updated meta-analysis," *Stroke*, vol. 38, pp. 1404–1410, 2007, doi: 10.1161/01.STR.0000260955.51401.cd.

[8] A. L. Ho, A. Mouminah, and R. Du, "Posterior cerebral artery angle and the rupture of basilar tip aneurysms," *PLoS ONE*, vol. 9, no. 10, p. e110946, Oct. 2014, doi: 10.1371/journal.pone.0110946.

[9] J. P. Greving *et al.*, "Development of the PHASES score for prediction of risk of rupture of intracranial aneurysms: A pooled analysis of six prospective cohort studies," *Lancet Neurol.*, vol. 13, no. 1, pp. 59–66, Nov. 2013, doi: 10.1016/S1474-4422(13)70263-1.

[10] M. Li, Z. Jiang, H. Yu, and T. Hong, "Size ratio: A morphological factor predictive of the rupture of cerebral aneurysm?" *J. Neurol. Sci.*, vol. 40, pp. 366–371, 2013, doi: 10.1017/S0317167100014323.

[11] N. Lv *et al.*, "Morphological and hemodynamic discriminators for rupture status in posterior communicating artery aneurysms," *PLoS ONE*, vol. 11, no. 2, p. e0149906, Feb. 2016, doi: 10.1371/journal.pone.0149906.

[12] M. J. Moghaddam and H. Soltanian-Zadeh, "Medical image segmentation using artificial neural networks," in *Methodological Advances and Biomedical Applications*, K. Suzuki, Ed. Rijeka, Croatia: InTech, 2010.

[13] N. Etminan *et al.*, "The unruptured intracranial aneurysm treatment score—A multidisciplinary consensus," *Neurology*, vol. 85, pp. 881–889, Aug. 2015.

[14] R. D. Millán, L. Dempere-Marco, J. M. Pozo, J. R. Cebral, and A. F. Frangi, "Morphological characterization of intracranial aneurysms using 3-D moment invariants," *IEEE Trans. Med. Imag.*, vol. 26, no. 9, pp. 1270–1282, Sep. 2007.

[15] M. L. Raghavan, B. Ma, and R. E. Harbaugh, "Quantified aneurysm shape and rupture risk," *J. Neurosurg.*, vol. 102, pp. 355–362, Feb. 2005.

[16] S. Kostopoulos *et al.*, "A Hybrid pixel-based classification method for blood vessel segmentation and aneurysm detection on CTA," *Comput. Graph.*, vol. 31, pp. 493–500, Jan. 2007.

[17] A. Chien, J. Sayre, and F. Vinuela, "Comparative morphological analysis of the geometry of ruptured and unruptured aneurysms," *Neurosurgery*, vol. 69, pp. 349–356, Mar. 2011.

[18] R. M. Haralick, K. Shanmugam, and I. H. Dinstein, "Textural features for image classification," *IEEE Trans. Syst., Man, Cybern.*, vol. SMC-3, no. 6, pp. 610–621, Nov. 1973.

[19] A. Kassner and R. E. Thornhill, "Texture analysis: A review of neurologic MR imaging applications," *Amer. J. Neuroradiol.*, vol. 31, pp. 809–816, May 2010.

[20] R. M. Haralick, "Statistical and structural approaches to texture," *Proc. IEEE*, vol. 67, no. 5, pp. 786–804, May 1979.

[21] C. J. Moran, "Aneurysmal subarachnoid hemorrhage: DSA versus CT angiography—Is the answer available?" *Radiology*, vol. 258, no. 1, pp. 15–17, 2011.

[22] C. J. Prestigiacomo *et al.*, "Predicting aneurysm rupture probabilities through the application of a computed tomography angiography–derived binary logistic regression model," *J. Neurosurg.*, vol. 110, pp. 1–6, Jan. 2009.

[23] I. Larrabide *et al.*, "Automated intracranial aneurysm isolation and quantification," in *Proc. 32nd Annu. Int. Conf. IEEE (EMBS)*, Buenos Aires, Argentina, Sep. 2010, pp. 2841–2844.

[24] X. Yang, M. C. Villa-Urio, R. Cardenes, J. M. Pozo, D. R. Hose, and A. F. Frangi, "Computer-aided detection of intracranial aneurysm in MR angiography," *J. Imag.*, vol. 24, no. 1, pp. 86–95, 2011.

[25] C. M. Hentschke, O. Beuing, R. Nickl, and K. D. Tönnies, "Automatic cerebral aneurysm detection in multimodal angiographic images," in *Proc. IEEE Nucl. Sci. Symp. Conf. Rec.*, Oct. 2011, pp. 3116–3120.

[26] M. W. K. Law and A. C. S. Chung, "Segmentation of intracranial vessels and aneurysms in phase contrast magnetic resonance angiography using multirange filters and local variances," *IEEE Trans. Image Process.*, vol. 22, no. 3, pp. 845–859, Mar. 2013.

[27] H. Liu, Y. Shao, D. Guo, Y. Zheng, Z. Zhao, and T. Qiu, "Cirrhosis classification based on texture classification of random features," *Comput. Math. Methods Med.*, vol. 2014, Feb. 2014, Art. no. 536308.

[28] I. Rahmany and N. Khlifa, "Detection of intracranial aneurysm in angiographic images using fuzzy approaches," in *Proc. IEEE IPAS Int. Image Process. Appl. Syst. Conf.*, Nov. 2014, pp. 1–6.

[29] F. Li-Dong and Y.-F. Zhang, "Medical image retrieval and classification based on morphological shape feature," in *Proc. 3rd Int. Conf. Intell. Netw. Intell. Syst.*, Nov. 2010, pp. 116–119.

[30] T. Y. So, R. Dowling, P. J. Mitchell, J. Laidlaw, and B. Yan, "Risk of growth in unruptured intracranial aneurysms: A retrospective analysis," *J. Clin. Neurosci.*, vol. 17, no. 1, pp. 29–33, 2010.

[31] K. Karunanithi, C.-J. Lee, Y. Zhang, and Y. Qian, "Risk stratification of cerebrovascular aneurysm using CFD—A review," in *Proc. 9th Int. Conf. CFD Minerals Process Ind. (CSIRO)*, Melbourne, VIC, Australia, 2012, p. 12.

[32] S. Dhar *et al.*, "Morphology parameters for intracranial aneurysm rupture risk assessment," *Neurosurgery*, vol. 63, no. 2, pp. 185–197, Aug. 2008.

[33] Accessed: Nov. 29, 2017. [Online]. Available: http://www.opencv.org/

[34] Accessed: Nov. 29, 2017. [Online]. Available: https://www.imagej.net/

[35] Accessed: Nov. 29, 2017. [Online]. Available: http://www.cs.waikato.ac.nz/ml/weka/

[36] Accessed: Nov. 29, 2017. [Online]. Available: http://www.accord-framework.net/docs/html/T_Accord_Imaging_Haralick.htm

[37] Accessed: Nov. 29, 2017. [Online]. Available: http://www.accord-framework.net/docs/html/T_Accord_Imaging_GrayLevelCooccurrenceMatrix.htm

[38] D. Backes *et al.*, "ELAPSS score for prediction of risk of growth of unruptured intracranial aneurysms," *Neurology*, vol. 88, no. 17, pp. 1600–1606, 2017.

[39] L.-D. Jou and M. E. Mawad, "Growth rate and rupture rate of unruptured intracranial aneurysm: A population approach," *BioMed. Eng.*, vol. 8, p. 11, Jun. 2009. [Online]. Available: http://www.biomedical-engineering-online.com/content/8/1/11

[40] N. Lin, A. Ho, N. Charoenvimolphan, K. U. Frerichs, A. L. Day, and R. Du, "Analysis of morphological parameters to differentiate rupture status in anterior communicating artery aneurysms," *PLoS ONE*, vol. 8, no. 11, p. e79635, Nov. 2013.

[41] N. K. Yoon, S. McNally, P. Taussky, and M. S. Park, "Imaging of cerebral aneurysms: A clinical perspective," *Neurovascular Imag.*, vol. 2, no. 1, p. 6, 2016.

[42] Y. Nomura *et al.*, "Performance improvement in computerized detection of cerebral aneurysms by retraining classifier using feedback data collected in routine reading environment," *J. Biomed. Graph. Comput.*, vol. 4, no. 4, p. 12, Oct. 2014.

[43] C. M. Hentschke, O. Beuing, H. Paukisch, C. Scherlach, M. Skalej, and K. D. Tönnies, "A system to detect cerebral aneurysms in multimodality angiographic data sets," *Med. Phys.*, vol. 41, Sep. 2014.

[44] T. Jerman, F. Pernuš, B. Likar, and Ž. Špiclin, "Blob enhancement and visualization for improved intracranial aneurysm detection," *IEEE Trans. Vis. Comput. Graphics*, vol. 22, no. 6, pp. 1705–1717, Jun. 2016.

[45] T. Jerman, F. Pernuš, B. Likar, Ž. Špiclin, and A. Chien, "Automatic cutting plane identification for computer-aided analysis of intracranial aneurysms," in *Proc. 23rd Int. Conf. Pattern Recognit. (ICPR)*, Cancún, México, Dec. 2016, pp. 1484–1489.

[46] S. Yang and B.-U. Lee, "Poisson-Gaussian noise reduction using the hidden Markov model in contourlet domain for fluorescence microscopy images," *PLoS ONE*, vol. 10, no. 9, p. e0136964, Sep. 2015.

[47] A. H. Hamad, H. O. Muhamad, and S. P. Yaba, "De-noising of medical images by using some filters," *Int. J. Biotechnol. Res.*, vol. 2, no. 2, p. e0136964, Jul. 2014.

[48] S. Pyatykh and J. Hesser. (Dec. 2015). "MMSE estimation for Poisson noise removal in images." [Online]. Available: https://arxiv.org/abs/1512.00717

[49] N. C. Hammadi and H. Ito, "Improving the performance of feedforward neural networks by noise injection into hidden neurons," *J. Intell. Robot. Syst.*, vol. 21, no. 2, pp. 103–115, 1998.

[50] M. Sabri and T. Kurita, "Effect of additive noise for multi-layered perceptron with autoencoders," *IEICE Trans. Inf. Syst.*, vol. E100-D, no. 7, pp. 1494–1504, Jul. 2017.

KHALID MAHMOOD MALIK received the Ph.D. degree from the Tokyo Institute of Technology in 2010. He was with Sanyo Electric Co., Japan, and DTS Inc., Japan, as Visiting Researcher and Project Manager of the Semantic Research Group, respectively. He has been an Assistant Professor with the School of Engineering and Computer Science, Oakland University, Rochester, MI, USA, since 2014. His research interests include medical image analytics, precision medicine-based decision support system, ontology-based information extraction, autonomous decentralized systems, and health information security.

SHAKEEL M. ANJUM has been an Assistant Professor with the Computer Science Department, FAST–National University of Computer and Emerging Sciences, Pakistan, since 2015. His research interests broadly include precision medicine, cloud computing, computer vision, and machine learning, and in specific, designing architecture of decision support system for detection and estimation of cerebral aneurysms and resolving unequivocal research problems involved in multimedia analytics in distributed computing environment.

HAMID SOLTANIAN-ZADEH received the B.S. degree (Hons.) in electrical engineering and the M.S. degree (Hons.) in electronics from the University of Tehran, Tehran, Iran in 1986, and the M.S.E. degree in electrical engineering and the Ph.D. degree in systems and bioelectrical sciences from The University of Michigan, Ann Arbor, MI, USA, in 1990 and 1992, respectively. Since 1988, he has been with the Department of Radiology, Henry Ford Health System, Detroit, MI, USA, where he is currently a Senior Scientist and the Director of the Medical Image Analysis Laboratory His research interests include medical imaging, signal and image processing and analysis, pattern recognition, and neural networks.

HAFIZ MALIK is currently an Associate Professor with the Electrical and Computer Engineering Department, University of Michigan-Dearborn. His research interests are image analysis, multimedia forensics, pattern recognition, information fusion, and biometric security.

GHAUS M. MALIK is currently the John R. Davis Chair and Executive Vice-Chair, Neurosurgery at Henry Ford Health System, Detroit, MI, USA. He specializes in cerebrovascular neurosurgery-especially aneurysms and arteriovenous malformations. His research interests include aneurysm rupture prediction, vasospasm, clinical outcomes of arteriovenous malformations (AVM), and genetic mechanisms for familial aneurysms and AVM.

● ● ●